Response of Mode Water and Subtropical Countercurrent to Greenhouse Gas and Aerosol Forcing in the North Pacific

WANG Liyi[1], LIU Qinyu[1], [*], XU Lixiao[1], and XIE Shang-Ping[2], [1]

1) *Physical Oceanography Laboratory and Key Laboratory of Ocean-Atmosphere Interaction and Climate in Universities of Shandong, Ocean University of China, Qingdao 266100, P. R. China*
2) *Scripps Institution of Oceanography, University of California at San Diego, La Jolla, CA 92093-0230, USA*

Abstract   The response of the North Pacific Subtropical Mode Water and Subtropical Countercurrent (STCC) to changes in greenhouse gas (GHG) and aerosol is investigated based on the 20th-century historical and single-forcing simulations with the Geophysical Fluid Dynamics Laboratory Climate Model version 3 (GFDL CM3). The aerosol effect causes sea surface temperature (SST) to decrease in the mid-latitude North Pacific, especially in the Kuroshio Extension region, during the past five decades (1950–2005), and this cooling effect exceeds the warming effect by the GHG increase. The STCC response to the GHG and aerosol forcing are opposite. In the GHG (aerosol) forcing run, the STCC decelerates (accelerates) due to the decreased (increased) mode waters in the North Pacific, resulting from a weaker (stronger) front in the mixed layer depth and decreased (increased) subduction in the mode water formation region. The aerosol effect on the SST, mode waters and STCC more than offsets the GHG effect. The response of SST in a zonal band around 40°N and the STCC to the combined forcing in the historical simulation is similar to the response to the aerosol forcing.

Key words   North Pacific; Subtropical Countercurrent; mode water; greenhouse gas; aerosol

1 Introduction

Increasing concentrations of the greenhouse gas (GHG) in the atmosphere are considered to be the major cause of global warming (Meehl *et al.*, 2007). On the other hand, the influence of atmospheric aerosol on climate is complex, including both direct radiative and indirect effects on cloud properties (Penner *et al.*, 2001). Anthropogenic aerosol effect partly offsets the GHG warming effect, and the inclusion of the former in a climate model can improve the model performance (Donner *et al.*, 2011).

The Subtropical Countercurrent (STCC) is a narrow eastward jet in the central North Pacific (20°N–30°N), flowing against the broad westward Sverdrup flow (Yoshida and Kidokoro, 1967). It is accompanied by a subsurface temperature and density front called the subtropical front (STF), in the thermal wind relationship with the STCC (Uda and Hasunuma, 1969; White *et al.*, 1978; Kobashi *et al.*, 2006). The STCC affects the atmosphere through its surface thermal effects, which can induce anomalous cyclonic wind curl and precipitation (Kobashi *et al.*, 2008).

The North Pacific mode waters, in particular, the Sub-

tropical Mode Water (STMW; Suga *et al.*, 1989) and the Central Mode Water (CMW; Nakamura, 1996; Suga *et al.*, 1997), play a key role in the formation and maintenance of the STCC and STF as illustrated by theoretical (Kubokawa, 1997, 1999), model (Takeuchi, 1984; Kubokawa and Inui, 1999; Yamanaka *et al.*, 2008), and observational (Aoki *et al.*, 2002; Kobashi *et al.*, 2006) studies. Using an ocean general circulation model (GCM), Kubokawa and Inui (1999) first illustrated the mechanisms for the STCC formation: mode waters of low potential vorticity (PV) on different isopycnals are subducted at different locations along the mixed layer depth (MLD) front, advected southward by the subtropical gyre, and eventually stacked up vertically to form a thick low-PV pool, which pushs the upper pycnocline upward. The slope of the upper pycnocline causes an eastward current near the surface. The hydrographic analysis of Kobashi *et al.* (2006) shows that the STCC is indeed anchored by mode waters beneath to the north. Thus mode waters are not only passive water masses but also exhibit an important dynamical effect on ocean circulation.

Based on the analysis of the output from the GFDL CM2.1 experiment under a CO_2 doubling, the surface water in the formation region and the core layer of STMW become warmer and fresher (Lee, 2009). Based on a set of the Intergovernmental Panel on Climate Change (IPCC) Forth Assessment Report (AR4) models, Luo *et al.* (2009)

* Corresponding author. Tel: 0086-532-66782556
  E-mail: liuqy@ouc.edu.cn

showed that in a warmer climate, mode waters are pro-
duced on lighter isopycnal surfaces and significantly re-
duced in volume. Using a 300-year control simulation
from the GFDL coupled model CM2.1, Xie *et al.* (2011)
showed that on decadal time scales, the dominant mode
of sea surface height (SSH) variability in the central sub-
tropical gyre (170˚E–130˚W, 15˚N–35˚N) is characterized
by the strengthening or weakening of the STCC as a re-
sult of variations in mode-water ventilation. This STCC
mode decays, owing to weakened mode waters in both
the mean state and variability (Xu *et al.*, 2012b), as CO_2
concentration increases in the 21st century.

Recent multi-model analysis confirmed that the weak-
ened mode waters and STCC are robust among the 17
Coupled Model Intercomparison Project Phase 5 (CMIP5)
models (Xu *et al.*, 2012a). Except for a recent study of
Suzuki and Ishii (2011) showing that STMW was warm-
ing and freshening during the period 1981–2007, no other
studies have reported significant changes in the mode
waters. Why are the mode waters and the STCC not re-
duced in the face of global mean temperature increasing?
One plausible hypothesis is that the aerosol effect may
offset the warming effect of GHG, but the aerosol effect
on the mode waters and STCC has not been investigated
in previous studies yet.

Observational analysis reveals that SST in the mid-
latitude North Pacific has decreased over the past five
decades (Fig.1). But in climate models, the response of
SST to increased CO_2 features a warming trend in the
North Pacific (See Fig.1; Xie *et al.*, 2010). Does the aero-
sol effect exceed the CO_2 effect on the SST in the North
Pacific? CMIP5 reported that global mean atmospheric
sulfate aerosol (SO_4) concentration increases slowly since
1850, and the increase accelerates in the latter half of the
20th century (Fig.2). Sharp increases in SO_4 concentra-
tion have been observed over Asia (70˚E–150˚E, 0˚–60˚N)
since 1950s. Aerosol optical depth (AOD) over East Asia
may have important impact on cloud and shortwave ra-
diation over the western North Pacific, which, in turn,
could induce SST response (Bao *et al.*, 2009). The SST
change in the North Pacific may further alter the proper-
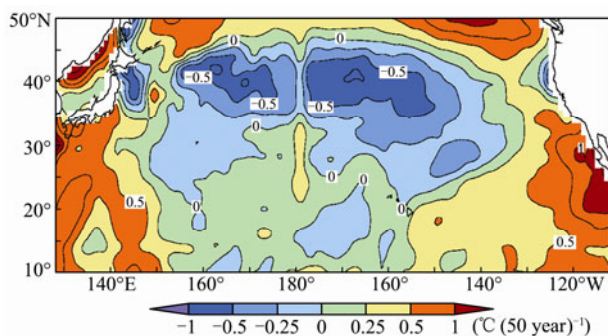ties of mode waters and the STCC.

Fig.1 The linear trend of SST (color in ℃ (50 year)$^{-1}$) in
the North Pacific during the past 56 years (1950–2005),
based on the HadISST data.

The present study, using the output from historical
all-forcing and single-forcing simulations and pre-indus-

trial control experiment of GFDL CM3, investigates the
aerosol cooling and GHG warming effects on the SST,
mode waters and the STCC in the North Pacific. The ma-
jor conclusion drawn from the study is that the aerosol
effect significantly exceeds the GHG effect over the past
five decades.

The rest of the paper is organized as follows. Section 2
briefly describes the model and simulations. Section 3
investigates the SST changes due to the aerosol and GHG
effects in the North Pacific. Section 4 studies the re-
sponses of the STCC, mode waters and related subduction
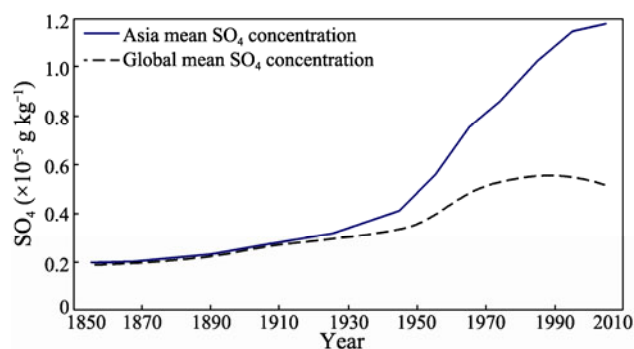processes to different forcing. Section 5 is a summary.

Fig.2 Atmospheric sulfate aerosol (SO_4) concentration
based on the CMIP5 recommended data.

2 Model and Simulations

This study uses the output from the National Oceanic
and Atmospheric Administration (NOAA) GFDL CM3,
one of the primary models from GFDL contributed to the
IPCC Fifth Assessment Report (AR5). The GFDL CM3 is
formulated with the same ocean and sea ice components
as the earlier CM2.1, and includes extensive development
of the atmosphere and land model components (Griffies
et al., 2011). Especially, aerosol-cloud interactions are
included in GFDL CM3, as documented by Donner *et al.*
(2011). The atmospheric component AM3 employs a
cubed-sphere implementation of a finite-volume dynami-
cal core with horizontal resolution of approximately 200
km. The ocean component MOM4 has a horizontal reso-
lution of $1.0˚×1.0˚$ and 50 layers, 22 of which are in the
upper 220 m. In the meridional direction the horizontal
resolution increases toward the equator, and the grid scale
becomes 1/3˚ between 30˚S and 30˚N.

A number of CM3 integrations were performed fol-
lowing the CMIP5 protocol (Taylor *et al.*, 2012), which
includes the pre-industrial control, a 5-member historical
ensemble, and 4 future scenarios (Representative Con-
centration Pathway 2.6, 4.5, 6.0 and 8.5). Detection and
attribution simulations were conducted to examine the
model's response to a subset of historical single forcing
(GHG forcing, natural forcing, aerosol forcing, and an-
thropogenic forcing), each consisting of 3 runs. Historical
and single-forcing simulations employ evolution of forc-
ing agents during the period 1860–2005, and each en-
semble member is initialized 50 years or 100 years apart
from the pre-industrial control experiment, which runs for

800 years with time-invariant radiative forcing agents fixed at the 1860 value.

The output of GHG forcing, aerosol forcing and historical all-forcing simulations is used in the present study. First, the output is processed to obtain the 1950–2005 mean and ensemble mean of each simulation from 3 members. The combined ensemble and time means allow for a robust signal from natural variability present in an individual ensemble member. As a reference, the 100–155 years averages are used from the pre-industrial control experiment (the first year of the control run is called 001 year).

3 SST Response to GHG and Aerosol Forcing

First the the climatology mean SST in the historical and single-forcing simulations and in pre-industrial control experiment (hereafter referred to as 'the control run') are compared (Fig.3). The SST response to the GHG forcing is opposite to that to the aerosol forcing. The SST difference between all forcing and the control run is close to zero in much of the North Pacific except in the mid-latitude regions (Fig.3c). The result shows that the SST response in the all forcing experiment is due to the combined effect of GHG and aerosol. But, in the zonal band of the mid-latitude North Pacific (40°N, 140°E–150°W), the SST rises by about 0.5℃–1.0℃ in the GHG forcing run (Fig.3a), and drops by 1.0℃–1.5℃ in the aerosol forcing run (Fig.3b) and by 0.5℃–1.0℃ in the all-forcing run (Fig.3c). Thus, in this zonal band, the SST response to all forcing is similar to the response to the aerosol forcing. Consequently, the aerosol effect is important in the observed SST dropping in the mid-latitude North Pacific, especially in the Kuroshio Extension region, during the past 56 years.
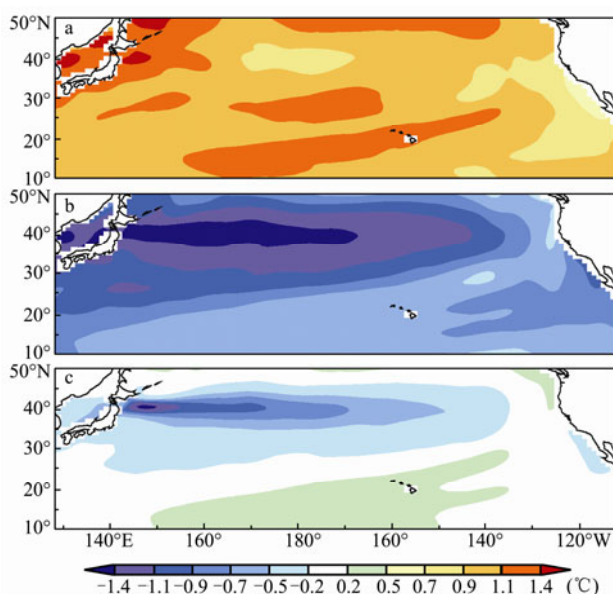

Fig.3 Climatology mean SST differences (1950–2005; color in ℃) in the North Pacific between (a) the GHG run, (b) the aerosol run, (c) the historical run and the control run, respectively.

4 STCC and Mode Waters Responses

Previous studies showed that the STCC is anchored by mode waters to the north (Kubokawa, 1999; Kobashi *et al.*, 2006; Yamanaka *et al.*, 2008; Xie *et al.*, 2011, Xu *et al.*, 2012a, b), and the changes in mode waters can be further traced upstream to those in the MLD and the subduction rate in the Kuroshio-Oyashio Extension (KOE) region (Xie *et al.*, 2011). In order to determine the physical mechanisms of the STCC change, the responses of the MLD, subduction, mode waters and STCC to different forcing are compared first, and then the relationship between the STCC and mode waters is investigated.

4.1 The MLD and Subduction

The MLD in CM3 reaches its seasonal maximum in the North Pacific in March. Generally, the March mixed layer is shallow in the southern subtropical gyre, but deepens northward and reaches its maximum in the mid-latitude regions. The water separating the deep mixed layer regions from the rest of the North Pacific is in a narrow transition zone called the MLD front (Xie *et al.*, 2000), which is a key to the formation of STMW and CMW (Kubokawa, 1999). The MLD front varies among four runs and is strongest in the aerosol forcing run with the largest subduction rate (Fig.4).

In the control run, there are two sub-regions where the MLD exceeds 400 m. On the south flank of the deepest MLD region are two subduction zones, where the MLD front intersects with the isopycnal surfaces of $25.5\sigma_\theta$ and $26.0\sigma_\theta$ and STMW and CMW are formed, respectively (Fig.4d). The GHG run, the aerosol runs and historical all-forcing run are compared with the control run respectively. In the GHG run (Fig.4a), the isopycnal outcrop lines move northwards, the MLD front becomes weaker, and the lateral induction decreases. In the aerosol run (Fig.4b), the situation is opposite because the mixed layer over the central North Pacific deepens by 80 m and the ocean surface cools (Fig.5b). In the historical all-forcing run (Fig.4c), the overall spatial structure of MLD is still similar but the local MLD maximum associated with CMW formation deepens compared to the control run. It indicates that the aerosol effect on MLD is greater than the GHG effect in the historical run.

The vertical section of potential temperature along the maximum change of MLD (175°W in Fig.5a; 180°E in Figs.5b and 5c) further clarifies the cause of the MLD change. In the GHG run, the warming is greater near the surface and decreases with depth. The resultant intensification of the upper ocean stratification inhibits winter convection, and shoals the mixed layer and isothermal layers (Fig.5d). In contrast, the potential temperature in the aerosol run decreases from the surface to about 400 m and the decreasing decays rapidly with depth. The reduced stratification leads to a MLD increase (Fig.5e). In the historical all-forcing run, the potential temperature decrease is similar to, but weaker than that in the aerosol

run, and the MLD deepens less accordingly (Fig.5f). Here the aerosol effect is again opposite to and surpasses the GHG effect on the MLD, and other forcing seems not to effect the MLD in Fig.5.
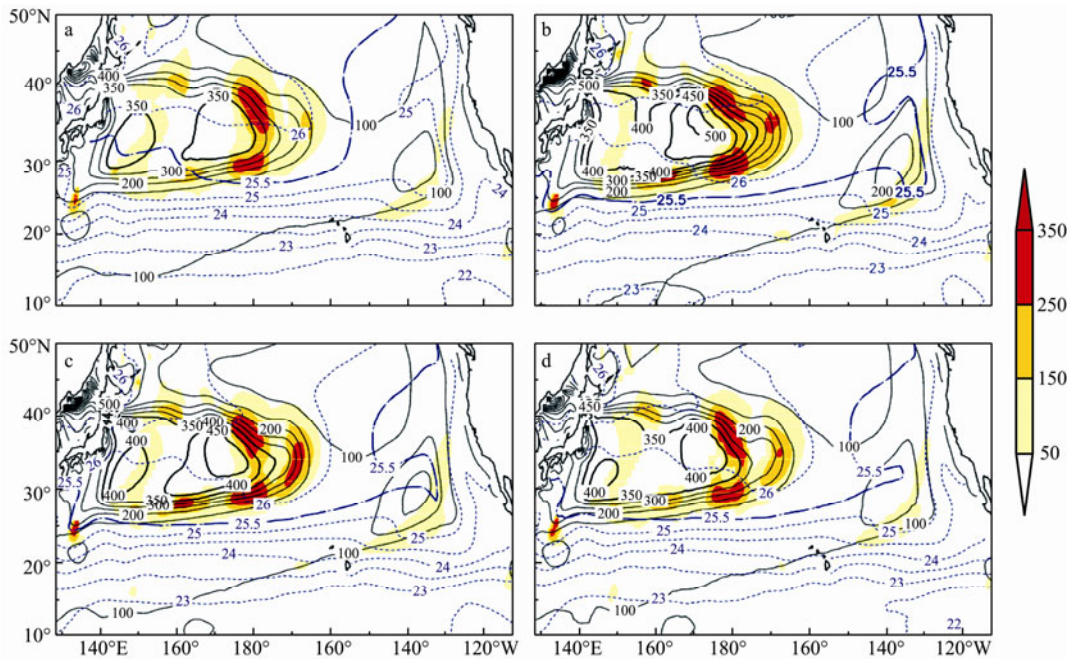

Fig.4 Mixed layer depth (black contour line and contour interval (CI)=50 m), outcrop line (blue dotted contour line (CI)= 0.5 kg m^{-3}) and lateral induction (color in m year^{-1}) in (a) the GHG run, (b) the aerosol run , (c) the historical run and (d) the control run during March.
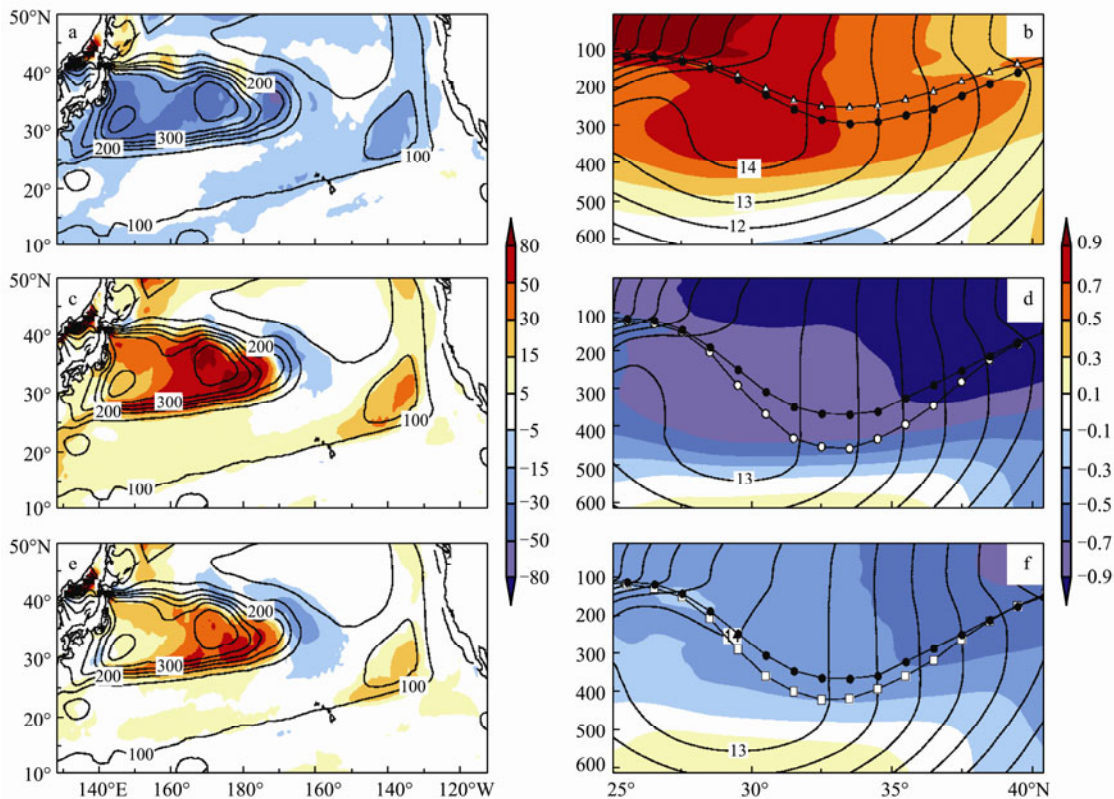

Fig.5 The differences in March mean MLD (shaded colors in m) between GHG run and control run (a) , between aerosol run and control run (b) and between historical run and control run (c), the superimposed contours (CI=50 m) denote MLD in the control run (a, b and c); The potential temperature differences (shaded colors in ℃) in meridional sections between the GHG run and control run (d, along 175˚W), between the aerosol run and control run (e, along 180˚E), between the historical run and control run (f, along 180˚E), respectively. The contours (CI=1℃) denote potential temperature and the black lines with solid circles denote MLD in the control run.

The lateral induction as a function of outcrop density is further analyzed by integrating the local positive lateral induction at a $\pm 0.05 \, \mathrm{kg \, m^{-3}}$ interval about each isopycnal layer over the area (140°E–160°W, 20°N–40°N), where the STMW and CMW form. Fig.6 compares the integral of the lateral induction. All runs show at least two distinct peaks of the lateral induction, which correspond to the two different outcrop densities for the STMW and CMW: $25.7\sigma_\theta$ and $26.1\sigma_\theta$ in the control run; $25.4\sigma_\theta$ and $26.0\sigma_\theta$ in the GHG run; $25.9\sigma_\theta$ and $26.5\sigma_\theta$ in the aerosol run; and $25.8\sigma_\theta$ and $26.3\sigma_\theta$ in the historical run. In the historical and control runs the core densities of the STMW and CMW are slightly higher than the observations, especially for the STMW with an observed typical core density of $25.4\sigma_\theta$ (Qiu and Huang, 1995; Suga *et al.*, 1997). As for the response to the GHG (aerosol) effect, less and lighter (more and denser) water appears in the cores of the STMW and the CMW in the GHG (aerosol) run.
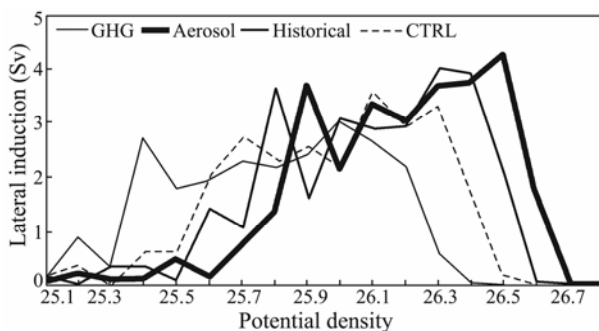

Fig.6 Lateral induction (March) for each density class in the North Pacific (140°E–160°W, 20°N–40°N) from different runs.

4.2 Mode Waters

The volume of the low-PV layer (less than 1.5×10^{-10} $\mathrm{m^{-1} \, s^{-1}}$) is calculated for each density class from 25.0 to $27.0 \, \mathrm{kg \, m^{-3}}$ between the layers at $\pm 0.05 \, \mathrm{kg \, m^{-3}}$ about an isopycnal layer in May. In order to exclude the formation area of the eastern subtropical mode water, the calculations are conducted in two regions (140°E–170°W, 20°N–40°N and 170°W–140°W, 30°N–40°N).

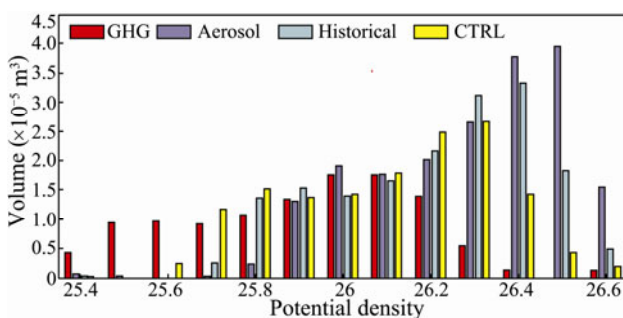As shown in Fig.7, corresponding to the STMW and the CMW, the low-PV water in different runs seems to

Fig.7 Total volume (m³) of the March low-PV (<1.5×10^{-10} $\mathrm{m^{-1} \, s^{-1}}$) layer for each density class in the North Pacific (140°E–170°W, 20°N–40°N and 170°W–140°W, 30°N–40°N) from different runs.

occur in two distinct potential density layers. Specifically, the major peaks of the STMW and the CMW volumes appear at $25.8\sigma_\theta$ and $26.3\sigma_\theta$ in the control run, $25.5\sigma_\theta$ and $26.0\sigma_\theta$ in the GHG run, $26.0\sigma_\theta$ and $26.5\sigma_\theta$ in the aerosol run, and $25.9\sigma_\theta$ and $26.4\sigma_\theta$ in the historical all-forcing run. The North Pacific mode waters (STMW and CMW) form on lighter isopycnal surfaces and decrease in volume in the GHG run, which is consistent with the results of Luo *et al.* (2009). The opposite is true for a cooler climate in the aerosol run. As a result that the aerosol effect surpasses the GHG effect, the North Pacific mode waters form on denser isopycnal surfaces and increase in volume in the historical all-forcing run.

4.3 STCC Response

Fig.8 shows the May climatological means of SSH and zonal current velocity at the 25-m level for four different runs. These runs all simulate on a basin scale the anti-cyclonic subtropical gyre circulation with an eastward jet (STCC) embedded in the central gyre where the Sverdrup zonal flow is sluggish. This STCC originates in the western Pacific around 20°N, intensifies and reaches its maximum velocity near 175°E, and then weakens gradually northeast of Hawaii. Compared to the control run (Fig.8d), the STCC in the GHG run weakens by $2 \, \mathrm{cm \, s^{-1}}$ (Fig.8a), but strengthens from $8 \, \mathrm{cm \, s^{-1}}$ to $10 \, \mathrm{cm \, s^{-1}}$ in the aerosol run (Fig.8b). In the historical run (Fig.8c), the STCC is stronger than in GHG run and similar to that in the aerosol run, because the aerosol effect exceeds the GHG effect.

4.4 Relationship Between Mode Waters and STCC

Fig.9 shows the eastward current speed, potential density, and PV for four different runs in a meridional section along 175°E in May. The STCC is confined above 200 m depth between 19°N–26°N. Because of the thermal wind balance it can be seen that the northward shoaling of the upper pycnocline is accompanied by a thick layer of low-PV water underneath in the north in all runs. In the control run (Fig.9d), the $26.2\sigma_\theta$ isopycnal layer begins to shoal northward from 20°N to 24°N and the $25.8\sigma_\theta$ isopycnal layer shows an even steeper northward shoaling, pushed by the low-PV water in between the $25.8–26.2\sigma_\theta$ layers. For the other runs (Figs.9a, 9b and 9c), the vertical structure of STCC and its relationship with mode waters do not change, indicating that the STCC is tied to mode waters. In the control run, the low-PV water core (less than $0.5 \times 10^{-10} \mathrm{m^{-1} s^{-1}}$) resides in between the $25.8–26.1\sigma_\theta$ layers with the STCC exceeding $8 \, \mathrm{cm \, s^{-1}}$. Compared to the control run, the low-PV water core weakens and moves to lighter isopycnal layers ($25.6–25.9\sigma_\theta$) with a decelerated STCC in the GHG run. By contrast, the low-PV water core intensifies and moves to denser isopycnal layers ($26.0–26.3\sigma_\theta$), and the STCC is accelerated with its maximum zonal velocity over $10 \, \mathrm{cm \, s^{-1}}$ in the aerosol run. In historical all-forcing run, the magnitudes of the low-PV water core and its residing isopycnal layers, $25.8–26.2\sigma_\theta$, fall in between the results of the GHG and aerosol runs, the maximum speed of the STCC still exceeds 10

cm s^{-1}, but the area with the speed exceeding $10\,\mathrm{cm\,s^{-1}}$ is smaller than in the aerosol run.

In order to clarify the relationship between mode waters and the STCC, the May PV distributions are calculated on the isopycnals from 25.0 to 27.0 kg m^{-3} at an interval of 0.1 kg m^{-3}. PV is selected on $25.9\sigma_\theta$ in the GHG run (Fig.10a), $26.3\sigma_\theta$ in the aerosol run (Fig.10b), $26.2\sigma_\theta$ in the historical run (Fig.10c), and $26.1\sigma_\theta$ in the control run (Fig.10d) to represent the mode waters core. Fig.10 shows that a weakened mode water causes the STCC to decelerate in the GHG run, whereas an enhanced mode water cause it to accelerate in the aerosol run as mentioned above.

Table 1 shows the regional averages of the eastward

current speed in the STCC core (140˚E–160˚W, 20˚N–25˚N), the positive lateral induction in subduction region (140˚E–160˚W, 25˚N–40˚N), and the volume of the low-PV water core with $\sigma_\theta < 26.5$ north of the STCC (140˚E–160˚W, 20˚N–30˚N) from different runs. In the aerosol run the lateral induction is the largest, the low-PV water and the STCC are the strongest. However, the results in the GHG run are just the opposite. In the historical run, the lateral induction rate, the volume of the low-PV water and the STCC speed are somewhere between the aerosol and GHG runs, but still larger than those in the control run, because the aerosol cooling effect is larger than the GHG warming effect.
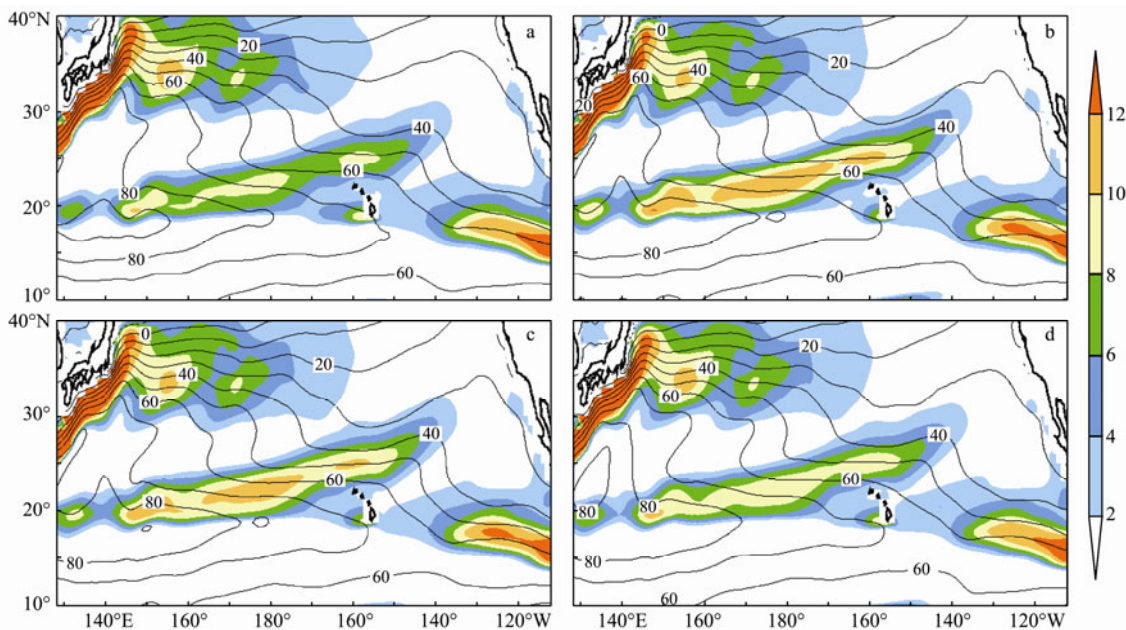

Fig.8 May climatological means of zonal current speed (color in cm s^{-1}) and SSH (CI=10 cm) over the North Pacific in (a) the GHG run, (b) the aerosol run, (c) the historical run, and (d) the control run, respectively.
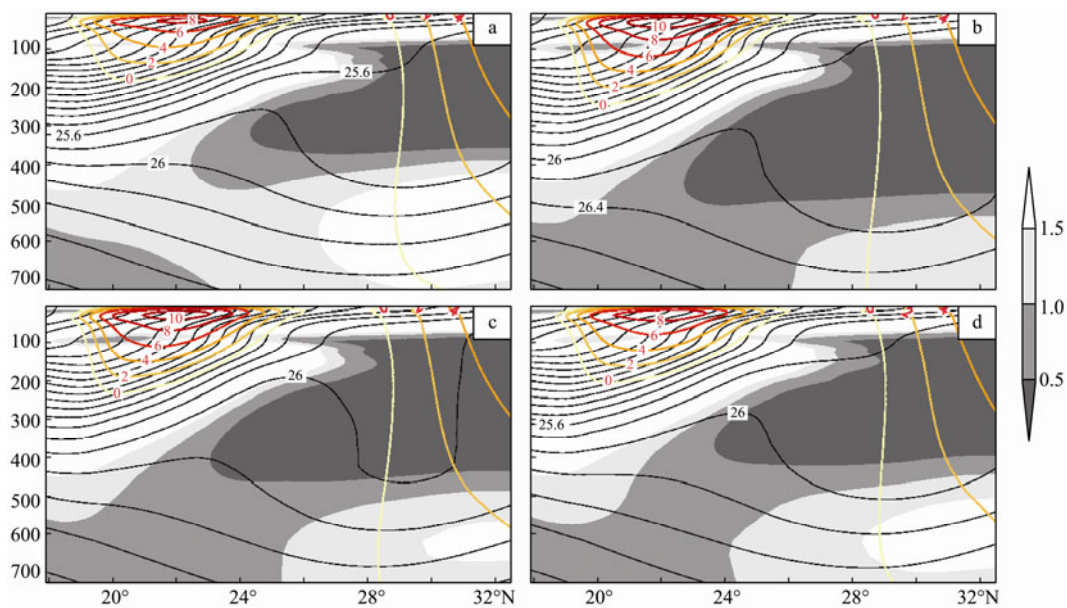

Fig.9 May **c**limatological means of eastward current speed (color contours at $2\,\mathrm{cm\,s^{-1}}$), potential density (black contours at 0.2 kg m^{-3} intervals), and PV (gray shading in $10^{-10}\,\mathrm{m^{-1}\,s^{-1}}$) for (a) the GHG run, (b) the aerosol run, (c) the historical run, and (d) the control run, respectively, in a meridional section along 175˚E.
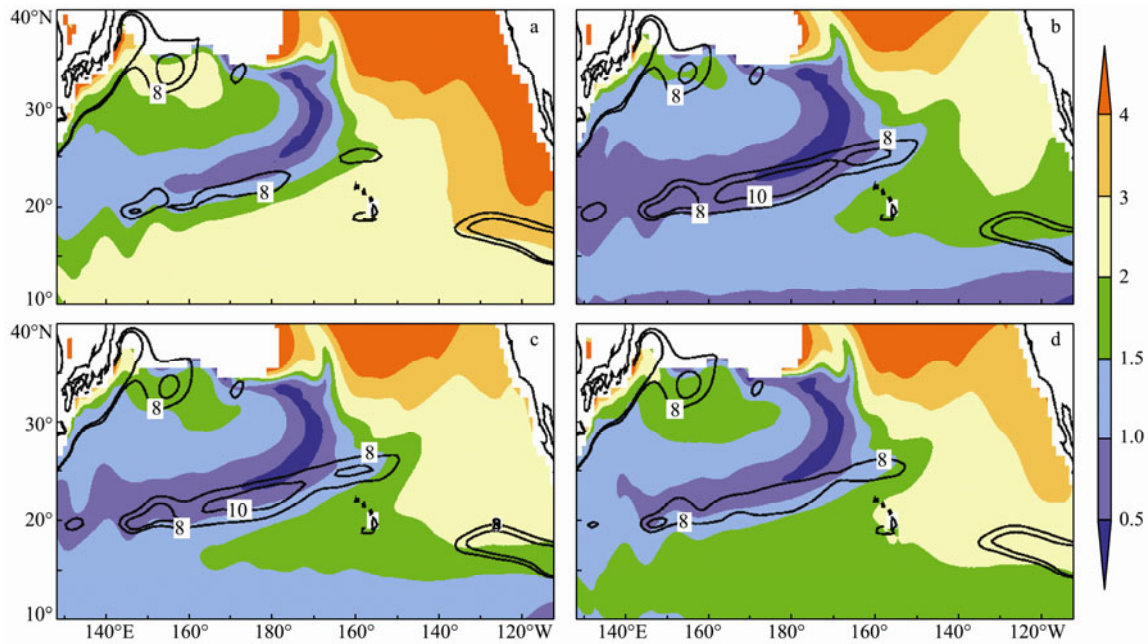
Fig.10 May climatological means of eastward current speed (>8 cm s^{-1} contours in cm s^{-1}) and PV (color in 10^{-10} m^{-1} s^{-1}) on (a) 25.9σ_θ in the GHG run, (b) 26.3σ_θ in the aerosol run, (c) 26.2σ_θ in the historical run, and (d) 26.1σ_θ in the control run in the North Pacific in May.

Table 1 The area-averaged values from different runs

Run	STCC speed (cm s^{-1})	Mode waters volume (10^{14} m^3)	Lateral induction (SV)
GHG	5.6	2.8	21.7
Aerosol	7.2	7.2	26.4
Historical	7.0	6.4	25.5
CTRL	6.2	4.3	23.4

5 Summary

The responses of the SST, mode waters and STCC to the GHG and aerosol effects are examined in the 20th century single-forcing and historical all-forcing simulations using GFDL CM3. The SST in the mid-latitude North Pacific increases in response to the GHG forcing, but decreases in response to the aerosol forcing. The model results show that the aerosol cooling effect is larger than the GHG warming effect, and the SST in the mid-latitude North Pacific experiences a net decreases in response to all-forcing in history. Thus, the aerosol effect appears to be a more important physical mechanism for the observed SST decreases in the North Pacific, especially in the Kuroshio Extending region, during the past 56 years (1950–2005). The GHG run corresponds to a more stratified upper ocean and a shoaled MLD while the aerosol run corresponds to a weakened ocean stratification and a deepened MLD. The maximum change in MLD appears in the KOE region where the mean MLD is the largest, and the MLD front and the subduction rate also experience changes (mainly by lateral induction). As a result of the decreased subduction rate and mixed layer density, less mode waters are formed on lighter isopycnals in the GHG run. By contrast, more mode waters are formed on denser isopycnals in the aerosol run, due to the increased subduction rate and mixed layer density. The southward advection of the weakened (strengthened) mode waters allows the upper pycnocline to rise less (more) and decelerates (accelerate) the STCC in response to the GHG (aerosol) forcing. In general, the effect of the aerosol forcing is larger than the effect of the GHG forcing, and the response of the STCC to all-forcing resembles that to the aerosol forcing in trend and spatial pattern, albeit weaker in magnitude.

One caveat from this modeling study is that the modeled mode waters and the STCC are too strong comparing with the observations, a bias common to CMIP5 models (Xu *et al.*, 2012a). The future scenarios of atmospheric composition call for an eventual decrease in aerosols but a continued increase in GHG. As a result, the GHG warming effect will dominate and cause a reduction in mode-water ventilation and weakening of the STCC in the 21st century (Xu *et al.*, 2012a, 2013). Further model improvements are necessary to better understand the response to anthropogenic forcing, and to obtain a more reliable projection of regional and global climate change.

References

Aoki, Y., Suga, T., and Hanawa, K., 2002. Subsurface subtropical fronts of the North Pacific as inherent boundaries in the ventilated thermocline. *Journal of Physical Oceanogra-*

phy, **32**: 2299-2311.

Bao, Z., Wen, Z., and Wu, R. G., 2009. Variability of aerosol optical depth over east Asia and its possible impacts. *Journal of Geophysical Research*, **114**, D05203, DOI: 10.1029/2008 JD010603.

Donner, L. J., Wyman, B. L., Hemler, R. S., Horowitz, L. W., Ming, Y., Zhao, M., Golaz, J. C., Ginoux, P., Lin, S. J., Schwarzkopf, M. D., Austin, J., Alaka, G., Cooke, W. F., Delworth, T. L., Freidenreich, S. M., Gordon, C. T., Griffies, S. M., Held, I. M., Hurlin, W. J., Klein, S. A., Knutson, T. R., Langenhorst, A. R., Lee, H. C., Lin, Y., Magi, B. I., Malyshev, S. L., Milly, P. C., Naik, V., Nath, M. J., Pincus, R., Ploshay, J. J., Ramaswamy, V., Seman, C. J., Shevliakova, E., Sirutis, J. J., Stern, W. F., Stouffer, R. J., Wilson, R. J., Winton, M., Wittenberg, A. T., and Zeng, F., 2011. The dynamical core, physical parameterizations, and basic simulation characteristics of the atmospheric component AM3 of the GFDL global coupled model CM3. *Journal of Climate*, **24**: 3484-3519.

Griffies, S. M., Winton, M., Donner, L. J., Horowitz, L. W., Downes, S. M., Farneti, R., Gnanadesikan, A., Hurlin, W. J., Lee, H. C., Liang, Z., Palter, J. B., Samuels, B. L., Wittenberg, A. T., Wyman, B. L., Yin, J., and Zadeh, N., 2011. The GFDL's CM3 coupled climate model: Characteristics of the ocean and sea ice simulations. *Journal of Climate*, **24**: 3520-3544, DOI: 10.1175/2011JCLI3964.1.

Kobashi, F., Mitsudera, H., and Xie, S. P., 2006. Three subtropical fronts in the North Pacific: Observational evidence for mode water-induced subsurface frontogensis. *Journal of Geophysical Research-Oceans*, **111**, C09033, DOI: 10.1029/2006JC003479.

Kobashi, F., Xie, S. P., Iwasaka, N., and Sakamoto, T. T., 2008. Deep atmospheric response to the North Pacific oceanic subtropical front in spring. *Journal of Climate*, **21**: 5960-5975.

Kubokawa, A., 1997. A two-level model of subtropical gyre and subtropical countercurrent. *Journal of Oceanography*, **53**: 231-244.

Kubokawa, A., 1999. Ventilated thermocline strongly affected by a deep mixed layer: A theory for subtropical countercurrent. *Journal of Physical Oceanography*, **29**: 1314-1333.

Kubokawa, A., and Inui, T., 1999. Subtropical countercurrent in an idealized ocean GCM. *Journal of Physical Oceanography*, **29**: 1303-1313.

Lee, H. C., 2009. Impact of atmospheric CO_2 doubling on the North Pacific Subtropical Mode Water. *Geophysical Research Letters*, **36**, L06602, DOI: 10.1029/2008GL037075.

Luo, Y., Liu, Q., and Rothstein, L. M., 2009. Simulated response of North Pacific Mode Waters to global warming. *Geophysical Research Letters*, **36**, L23609, DOI: 10.1029/2009GL040906.

Meehl, G. A., Stocker, T. F., Collins, W. D., Friedlingstein, P., Gaye, A. T., Gregory, J. M., Kitoh, A., Knutti, R., Murphy, J. M., Noda, A., Raper, S. C. B., Watterson, I. G., Weaver, A. J., and Zhao, Z. C., 2007. Global climate projections. In: *Climate Change 2007: The Physical Science Basis. Contribution of Working Group I to the Fourth Assessment Report of the Intergovernmental Panel on Climate Change*. Solomon, S. *et al.*, eds., Cambridge University Press, 747-845.

Nakamura, H., 1996. A pycnostad on the bottom of the ventilated portion in the central subtropical North Pacific: Its distribution and formation. *Journal of Oceanography*, **52**: 171-188.

Penner, J. E., Andreae, M., Annegarn, H., Barrie, L., Feichter, J., Hegg, D., Jayaraman, A., Leaitch, R., Murphy, D., Nganga, J., and Pitari, G., 2001. Aerosols, their direct and indirect effects. *Intergovernmental Panel on Climate Change, Report to IPCC from the Scientific Assessment Working Group (WGI)*, Cambridge University Press, 289-348.

Qiu, B., and Huang, R. X., 1995. Ventilation of the North Atlantic and North Pacific: Subduction versus obduction. *Journal of Physical Oceanography*, **25**: 2374-2390.

Suga, T., Hanawa, K., and Toba, Y., 1989. Subtropical mode water in the 137˚E section. *Journal of Physical Oceanography*, **19**: 1605-1618.

Suga, T., Takei, Y., and Hanawa, K., 1997. Thermostad distribution in the North Pacific subtropical gyre: The central mode water and the subtropical mode water. *Journal of Physical Oceanography*, **27**: 140-152.

Suzuki, T., and Ishii, M., 2011. Long term regional sea level changes due to variations in water mass density during the period 1981–2007. *Geophysical Research Letters*, **38**, L21604, DOI: 10.1029/2011GL049326.

Takeuchi, K., 1984. Numerical study of the subtropical front and the subtropical countercurrent. *Journal of Oceanographical Society of Japan*, **40**: 371-381.

Taylor, K. E., Stouffer, R. J., and Meehl, G. A., 2012. An overview of CMIP5 and the experiment design. *Bulletin of American Meteorological Society*, **93** (4): 485-498, DOI: 10.1175/BAMS-D-11-00094.1.

Uda, M., and Hasunuma, K., 1969. The eastward subtropical countercurrent in the western North Pacific Ocean. *Bulletin of American Meteorological Society*, **25**: 201-210.

White, W. B., Hasunuma, K., and Solomon, H., 1978. Largescale seasonal and secular variability of the subtropical front in the western North Pacific from 1954 to 1974. *Journal of Geophysical Research*, **83**: 4531-4544.

Xie, S. P., Deser, C., Vecchi, G. A., Ma, J., Teng, H., and Wittenberg, A. T., 2010. Global warming pattern formation: Sea surface temperature and rainfall. *Journal of Climate*, **23**: 966-986.

Xie, S. P., Kunitani, T., Kubokawa, A., Nonaka, M., and Hosoda, S., 2000. Interdecadal thermocline variability in the North Pacific for 1958–1997: A GCM simulation. *Journal of Physical Oceanography*, **30**: 2798-2813.

Xie, S. P., Xu, L., Liu, Q., and Kobashi, F., 2011. Dynamical role of mode water ventilation in decadal variability in the central subtropical gyre of the North Pacific. *Journal of Climate*, **24**: 1212-1225.

Xu, L. X., Xie, S. P., and Liu, Q., 2012a. Mode water ventilation and subtropical countercurrent over the North Pacific in CMIP5 simulations and future projections. *Journal of Geophysical Research–Oceans*, **117**, C12009, DOI: 10.1029/2012 JC008377

Xu, L. X., Xie, S. P., and Liu, Q. Y., 2013. Fast and slow response of the North Pacific Mode Water and subtropical countercurrent to global warming. *Journal of Ocean University of China*, **12** (2), DOI: 10.1007/s11802-013-2189-6.

Xu, L. X., Xie, S. P., Liu, Q., and Kobashi, F., 2012b. Response of the North Pacific subtropical countercurrent and its variability to global warming. *Journal of Oceanography*, **68**: 127-137, DOI: 10.1007/s10872-011-0031-6.

Yamanaka, G., Ishizaki, H., Hirabara, M., and Ishikawa, I., 2008. Decadal variability of the Subtropical Front of the western North Pacific in an eddy-resolving ocean general circulation model. *Journal of Geophysical Research*, **113**, C12027, DOI: 10.1029/2008JC005002.

Yoshida, K., and Kidokoro, T., 1967. A subtropical countercurrent in the North Pacific–An eastward flow near the Subtropical Convergence. *Journal of Oceanographical Society of Japan*, **23**: 88-91.

(Edited by Xie Jun)